

One of the Scenarios for Supershear Earthquakes

A. M. Budkov¹ and S. B. Kishkina^{1*}

¹ *Sadovsky Institute for Dynamics of Geospheres, Russian Academy of Sciences, Moscow, 119334 Russia*

* *e-mail: KishkinaS@idgras.ru*

Received July 21, 2023; revised September 25, 2023; accepted September 26, 2023

Abstract—This paper is a part of the study on the rupture propagation and seismic wave emission during the movement along the fault, whose fracture surface in different regions is made of geomaterials with different frictional properties. The slip surface of the fault is frictionally heterogeneous. It contains weakening zones (asperities), strengthening zones (barriers), and “background” zones that are almost neutral with respect to velocity and displacement. The scenario of a seismogenic rupture is determined precisely by the presence, number, and size of such zones with different dynamics of frictional characteristics. The study deals with the mechanics of supershear earthquakes, in which the rupture propagates with an unusually high velocity exceeding the shear wave velocity of the medium. Numerical simulation results confirm the existence of two different mechanisms governing the transition of an earthquake to the supershear regime. A model of the so-called “weak” fault is considered, for which the rupture velocity continuously increases from the sub-Rayleigh velocity C_R to the shear wave velocity C_s and quickly exceeds it without any jump. This scenario is typical for faults with the measure of strength S under 0.8. The solved problem is not only of fundamental importance for understanding the earthquake mechanics, but also can find application in engineering seismology and the study of earthquake-induced rupture processes, because unlike an ordinary earthquake, supershear or fast ruptures cause strong shaking at a much greater distance from the source of the event (from the fault). This is confirmed by direct data on near-field ground motion obtained in recent years by research groups from different countries.

Keywords: supershear earthquake, earthquake source, fault, rupture velocity, numerical simulation, frictional behavior, asperity, weak fault

DOI: 10.1134/S1029959924040064

1. INTRODUCTION

The investigation of rupturing during an earthquake is intended to bring us significantly closer to the understanding of the earthquake process. One of the important tasks is to study the mechanics of earthquakes with an unusually high rupture velocity V_r exceeding the shear wave velocity (Rayleigh wave velocity C_R). Though the determination of the earthquake rupture velocity V_r is highly inaccurate, it was believed to average between 1100 and 3100 m/s. This is also consistent with the classical ideas [1, 2]. However, it is currently known that the velocity of propagation of a rupture (primarily of a strike-slip (type II) fault) can exceed the C_R value [3–8], which has long been considered the maximum possible crack velocity [1], and reach the compression wave velocity. In geophysical literature, such phenomena are referred to as supershear or infrasonic earthquakes.

In the last few decades, considerable interest has been shown in this field. The problem is not only of fundamental importance for understanding the earthquake mechanics, but also can find applications in engineering seismology and the study of earthquake-induced rupture processes. The fact is that, unlike an ordinary earthquake, supershear or fast ruptures cause strong shaking at a much greater distance from the source of the event (from the fault). Vibrations produced by a supershear earthquake are much richer in higher frequencies [3, 6] because, in the train of shear waves at the formed flat fronts, similar to Mach fronts, the amplitude of ground vibrations decays much more slowly than during “normal” sub-Rayleigh ruptures [9]. The described earthquake scenario increases the risk of such events: they are potentially more destructive than other earthquake types and should be taken into account, for example, when predicting/estimating peak ground accelerations [10].

Along with indirect evidence based on the seismic data analysis [2, 3, 10, 11], there are direct data on the near-field ground motion, which confirm that the earthquake reaches the ultra-high velocity [12–15]. Thus, during the 2018 M_w 7.5 earthquake in Palu (Indonesia), the high-frequency (1 Hz) GPS station recorded the particle velocity (≈ 1.0 m/s) parallel to the fault exceeding the shear wave velocity in the host medium (≈ 0.7 m/s) [16].

It is often reported that the sub-Rayleigh-to-supershear transition is controlled by the Burridge–Andrews mechanism. This mechanism predicts the direct nucleation of a secondary crack (daughter crack) ahead of the front of the main crack where the shear stress reaches peak values [5, 17, 18].

However, the transition to the supershear regime is not always accompanied by the formation of a daughter crack. The numerical experiment on simulation of another scenario of a supershear rupture, without a secondary crack, will be detailed below.

2. SUPERSHEAR EARTHQUAKES

Until recently, supershear earthquakes have very rarely been studied. However, the analysis of a large number of events for which rupture characteristics were available finally confirmed that such fast ruptures were in fact much more common than recognized before [19]. In most cases, the rupture velocity is estimated from low-frequency teleseismic observations, which makes it possible to estimate only the average rupture velocity during the process in the source. When the analysis of near-field records is available, seismological analysis methods can accurately estimate the arrival time of high-frequency compression waves emitted by each fault segment. Consequently, inversion of seismic records received by several dense seismic networks can give fairly accurate values of the rupture velocity. A highly detailed determination of kinematic coseismic displacements is possible based on the data from global navigation satellite systems using remote sensing techniques. As a result, it was convincingly demonstrated that different fault segments can rupture at different velocities, and a part of the rupture can propagate faster than the shear wave velocity of the host rocks (e.g. [2, 7, 10, 12, 13, 20]). At the same time, it was noted in [7] (and repeatedly confirmed by the subsequent estimates) that supershear earthquakes occur

predominantly during strike-slip faults (as opposed to thrusts and dip-slip faults).

Thus, the authors of [2] analyzed data on 96 earthquakes with magnitudes M_w from 6.4 to 8.1 and revealed that 23 events had the average rupture velocity in the range from 3100 to 4500 m/s. The analysis of 86 earthquakes with the magnitude $M_w \geq 6.7$ made in [20] showed about 12 supershear events with rupture velocities from 4500 to 6200 m/s, including four oceanic earthquakes. In the past decade, a number of strong earthquakes were classified as supershear earthquakes. Among them is the 2008 M_w 7.9 earthquake in Wenchuan (China) [21], 2013 M_w 6.7 deep earthquake in the Sea of Okhotsk [22], 2013 M_w 7.5 earthquake in Alaska [23], 2018 M_w 7.5 earthquake in Palu (Indonesia) [16, 24], and Caribbean earthquakes (2018 M_w 7.5 and 2020 M_w 7.7) [20]. The data recorded during the 2021 M_w 7.4 earthquake in Qinghai Province, China allowed identifying the Mach wave generated by supershear rupture. The authors of [13] showed the asymmetry of rupture velocities and recorded the velocity about 3.67 km/s in one of the fault sections (3.8 km/s according to the data from [12]).

A destructive series of earthquakes with the magnitudes M_w 7.9 and M_w 7.6 occurred in 2023 in Southeastern Turkey near the northwestern border of Syria were also classified as supershear events [14, 15, 25]. This probably predetermined a large-scale scenario, being unexpected based on the historical data and known tectonic conditions. All previous earthquakes had the magnitude range ~ 6.8 – 7.2 , and none of them covered several segments of the East Anatolian Fault at once, unlike in 2023. Analysis of the near-field seismic records and development of dynamic inversion models for a rupture point to spatially inhomogeneous velocities during the Turkish earthquake [14]. There is a dense network of ground motion stations in this region, and their data will certainly be carefully processed further: the earthquakes were registered by almost three hundred strong-motion stations [26]. However, primary analysis has already confirmed that the rupture that began on the feathering fault reached the supersonic velocity before it caused an earthquake on the East Anatolian Fault [15].

Such estimation is important not only for the analysis of a specific catastrophic event, but also for assessing the possibility of recurrence of a similar scenario in another complex active fault system.

3. MECHANICS OF SUPERSHEAR EARTHQUAKES

The mechanics of transition of an earthquake to the supershear regime is related to the presence of regions with different frictional properties on the slip surface of the fault. A fairly detailed overview of the recent studies on sliding along faults was made in [27]. Here we only mention briefly the frictional heterogeneity of the slip surface, which includes weakening zones (asperities), strengthening zones (barriers), and “background” zones, which are almost neutral with respect to velocity and displacement [1, 28–31, etc.]. The scenario of a seismogenic rupture is determined precisely by the presence of such zones with different dynamics of frictional characteristics. A dynamic rupture is always initiated in the weakening zone. Its velocity decreases in the background zone and increases again on meeting the next weakening spot [32]. Strengthening zones can arrest sliding. A necessary condition for transition to a supershear rupture is the presence of a sufficient number of stress concentration zones in weakening zones (asperities). Heterogeneity of the contact surface governs the appearance of intervals of decrease and increase in the rupture velocity. At each dynamic rupture event, the fault sections that were previously displaced during the creep process are repeatedly destroyed. This increases the probability of supershear ruptures in older fault sections since the macroslip surface becomes smoother in mature faults: the characteristic sizes of zones with friction weakening properties increase, and the effective strength in these fault sections decreases [18, 27].

As already noted, the propagation of the so-called “daughter” crack has long been taken to be the main scenario of a supershear rupture [33]. In this case, the stress peak appears ahead of the front of the primary fault/crack, which gradually increases until the local strength of the fault is exceeded. As a result, a secondary crack is formed, which is separate from the main fault. The leading front of the daughter crack begins as an unstable supershear rupture, which then rapidly accelerates into a stable supershear rupture. The trailing front quickly coalesces with the main rupture, turning the entire crack to a supershear one. The condition for occurrence of a supershear rupture is shear-induced weakening of the contact surface and a sufficient level of background stresses [33, 34].

Recent simulation results point to an alternative way of passing to a supershear rupture. The special feature of this scenario is that the rupture immediately turns to the supershear regime, without the stage of

formation of a daughter crack. Such a scenario has not been studied before since it was believed that the propagation of a stationary singular crack in the range between the Rayleigh and shear wave velocities was theoretically impossible. However, today it is known that, in most cases, the rupture front smoothly but very quickly achieves the velocity range $[C_R, C_s]$ (the former “forbidden” velocity region) [6, 17].

To trace such rupture evolution from sub-Rayleigh to compression wave velocities, we carried out numerical experiments, which will be discussed below.

4. CALCULATION METHOD

The problem of rupture propagation along a model fault between the two infinite half-spaces was solved in a two-dimensional formulation. The fault was modeled by pure shear propagating along the contact plane between the two homogeneous blocks. Calculations were performed using a two-dimensional software package based on the Lagrangian numerical method “Tensor” [35]. The equations describing the motion and stress state of a solid in the Cartesian coordinate system have the form

$$\begin{aligned} \frac{d\rho}{dt} + \rho \operatorname{div} \mathbf{v} &= 0, \quad v_x = \frac{dx}{dt}, \quad v_y = \frac{dy}{dt}, \\ \rho \frac{dv_x}{dt} - \frac{\partial s_{xx}}{\partial x} - \frac{\partial s_{xy}}{\partial y} + \frac{\partial P}{\partial x} &= 0, \\ \rho \frac{dv_y}{dt} - \frac{\partial s_{yy}}{\partial y} - \frac{\partial s_{xy}}{\partial x} + \frac{\partial P}{\partial y} &= \rho g, \\ \rho \frac{d\varepsilon}{dt} - s_{xx} \dot{\varepsilon}_{xx} - s_{yy} \dot{\varepsilon}_{yy} - s_{zz} \dot{\varepsilon}_{zz} - 2s_{xy} \dot{\varepsilon}_{xy} - \frac{P}{\rho} \frac{d\rho}{dt} &= 0, \end{aligned} \tag{1}$$

where t is the time, x , y , and z are the coordinates (the x and y axes lie in the plane of symmetry of the problem, and the z axis is perpendicular to this plane), ρ is the density, v_x and v_y are the components of the velocity vector \mathbf{v} , g is the gravitational constant, P is the pressure, s_{ij} is the stress tensor deviator, $\dot{\varepsilon}_{ij}$ is the strain rate tensor deviator, ε is the specific internal energy, and d/dt is the Lagrangian time derivative:

$$\frac{df}{dt} = \frac{\partial f}{\partial t} + (\mathbf{v}, \nabla) f.$$

The system of equations of motion is closed by stress–strain relations.

The influence of the gravity field and the related lithostatic stresses, as well as strength characteristics of the geomaterial, is given no consideration. Therefore, the block material is described by the relations

of ideal elasticity, and the gravitational constant g in the system of Eqs. (1) is set to zero.

Within the Lagrangian approach, the process of shear deformation of discontinuities is studied by specifying a special boundary condition at the block contact, namely, a slip contact boundary. In this case, the tangential stress tensor components at the contact boundary are determined using the model of shear deformation of the block contact selected for the calculation of this boundary section.

The field of homogeneous shear stresses $\sigma_{xy} = \tau_0$ was set as the initial conditions in the blocks. The heterogeneous slip surface was modeled by alternating zones of two types: zones characterized by rapid friction weakening of the contact during shear (FW, friction weakening), and passive zones, i.e. zones of background stress $\tau = \tau_0$ with a constant shear resistance (FS, friction stable). This is the case in many tectonic conditions, when during the “interseismic” period, potentially active zones (asperities) are fixed and have zero displacement, and passive zones are in the state of slow creep [18, 27]. Friction in the velocity weakening zones was specified by the relation

$$\tau = T(\Delta u) \operatorname{sgn}\left(\frac{\partial \Delta u}{\partial t}\right), \quad \frac{\partial \Delta u}{\partial t} \neq 0, \quad (2)$$

where

$$T(\Delta u) = \begin{cases} \tau_u - \frac{(\tau_u - \tau_f)\Delta u}{d_0}, & \Delta u < d_0, \\ \tau_f, & \Delta u \geq d_0, \end{cases}$$

u is the relative displacement of the fault sides, τ_u is the peak frictional strength, τ_f is the residual frictional strength, and d_0 is the sliding weakening amplitude (the displacement at which friction decreases from the peak to residual value). During stable sliding, shear stresses at the contact are always equal to τ_f .

The length was normalized by using the parameter L_c corresponding to the critical half-length of the Griffith crack (the fault propagation is symmetrical):

$$L_c = \frac{8}{\pi} \frac{\mu(\lambda + \mu)}{\lambda + 2\mu} \frac{G}{(\tau_0 - \tau_f)^2}.$$

Here λ and μ are the Lamé coefficients, $G = 1/4(\tau_u - \tau_f)d_0$ is the effective energy of crack formation, and τ_0 is the background shear stress.

The model parameters were set as follows: density $\rho_0 = 2.992 \times 10^3 \text{ kg/m}^3$, Poisson’s ratio $\nu = 0.25$, longitudinal wave velocity $C_p = 6 \text{ km/s}$, shear wave velocity $C_s = 3.46 \text{ km/s}$, and Rayleigh wave velocity $C_R = 3.18 \text{ km/s}$. The friction model parameters were $\tau_f = 55.2 \text{ MPa}$ and $d_0 = 48 \text{ mm}$. Background stresses

were set to $\tau_0 = 73.8 \text{ MPa}$, and the parameter τ_u depends on the parameter S given by

$$S = \frac{\tau_u - \tau_0}{\tau_0 - \tau_f}. \quad (3)$$

As can be seen, the parameter S is the ratio of the stress that should be accumulated to achieve the peak frictional strength to the stress drop. In fact, S is a dimensionless measure of the fault strength, by which it is convenient to characterize the stress state of the contact. From (3) it is easy to see that the lower the ratio τ_f/τ_u (the more “brittle” the fault), the lower the average stress τ_0/τ_u at which the transition to a supershear rupture can occur. In our calculations, the parameter S varied in the range $0.4 < S < 0.8$, i.e. we studied relatively “weak” faults as compared to the range $0.8\text{--}0.9$, which falls within the interval $0.8 \leq S < 1.8$ of “strong” faults (calculations for this interval were made in [18]). At $S \geq 1.8$, the rupture velocity remains below the Rayleigh wave velocity, and no transition of the fault to the supershear regime occurs [9, 17, 18, 33, 34].

Further, all characteristic sizes and times will be given in relative units: length $\hat{L} = L/L_c$ and time $\hat{t} = tC_s/L_c$, respectively. The size of the computational domain $\hat{\Sigma}$ varied from 120×120 to 180×180 in different calculations. A uniform computational grid with the cell size $\hat{l} = 0.015 \times 0.015$ was used.

In accordance with the recommendations of [33], the crack propagation in a small region \hat{L}_0 of the model fault (the parameter \hat{L}_0 was chosen equal to 4) was initiated by setting a stress drop propagating at the velocity $V_{r0} = 0.6C_s$. For this purpose, the grid point was artificially assigned a displacement 10% higher than the threshold value u_0 , at which friction reaches the background stress τ_0 . Calculations showed [18] that the stress drop zone should be of sufficient size; at $\hat{L}_0 \leq 3$, the rupture process is arrested in the immediate vicinity of the initiation site.

5. CALCULATION RESULTS

5.1. Homogeneous Contact Surface

In this series of calculations, the fault was modeled as a homogeneous contact surface between two blocks. Let us consider “dynamic” stresses arising during the propagation of the simulated rupture, without taking into account background shear stresses τ_0 . Figure 1 shows the spatial distribution of shear stresses σ_{xy} at the initial stage of the supershear rupture propagation ($\hat{t} = 15.1$, $S = 0.4$, $\tau_u = 81.24 \text{ MPa}$).

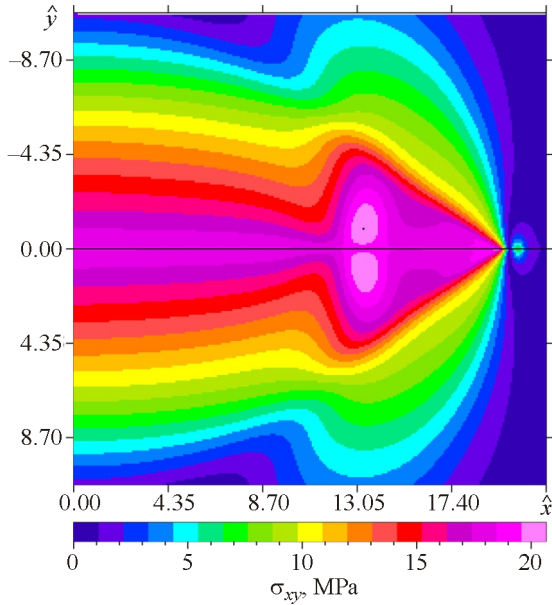


Fig. 1. Spatial distribution of shear stresses σ_{xy} at the initial stage of the supershear rupture propagation ($\hat{t} = 15.1$, $S = 0.4$). The x axis lies in the contact plane, and the y axis is perpendicular to this plane (color online).

A small zone of increased shear stresses is identified near the rupture front (Fig. 1). Analysis of the velocity vector fields shows that this zone is associated with the characteristic vortex motion of the medium. It is in this zone that the rupture starts, regardless of the further regime of its propagation.

Within the used friction model, differential motion along the fault is initiated under the condition [18]

$$\sigma_{xy} \geq \tau_u = \tau_0 + \Delta\tau. \quad (4)$$

In the sub-Rayleigh regime, condition (4) is satisfied only at the shear wave front: the moment of ful-

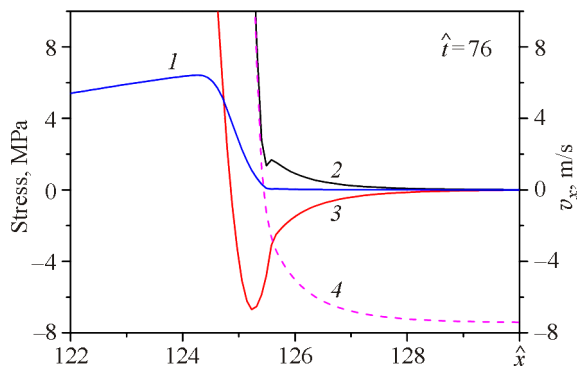


Fig. 2. Spatial distribution of the velocity component v_x (1) tangential to the interface, tangential σ_{xx} (2) and shear σ_{xy} stress tensor components (3), and parameter F (4) over the contact surface near the rupture initiation site at the time $\hat{t} = 76$ (color online).

fillment of this condition will be called the “differential motion start”. It is at this moment that the rupture begins to form.

The start of differential motion is illustrated in Fig. 2. It shows the distributions of the tangential velocity component u_x , tangential σ_{xx} and shear stress tensor components σ_{xy} on the contact surface near the rupture initiation site (compressive stresses σ_{xx} are thought to be positive). The dashed line in Fig. 2 shows the variation in the parameter $F(x) = (\Delta\sigma_{xx}(x) - \sigma_{xy}(x)) - (\tau_u - \tau_0)$, where $\Delta\sigma_{xx}$ is the difference in the tangential stress tensor components in neighboring cells of the computational grid at the slip boundary. The first term in the relation for $F(x)$ represents the total dynamic shear stress acting on a boundary point of the computational grid, and the second is the threshold stress that should be exceeded for differential motion to start. Thus, the transition of the function $F(x)$ from $F(x) < 0$ to $F(x) > 0$ is a condition for the beginning of differential motion, i.e. start of a rupture. Calculation data show that the main contribution to the necessary level of dynamic stresses for the rupture start is made by shear stresses σ_{xy} (~80%).

Hodographs of the starting moments of differential motion by the criterion $u = 0.1$ m/s are shown in Fig. 3. Dependences of the rupture start velocity C_f on the distance at different parameters S are shown in Fig. 4. Two types of transition are clearly distinguished for high and low S . At $S < 0.8$ (curves 1–3 in Fig. 4), a direct transition from the sub-Rayleigh to supershear rupture occurs: once started, the rupture gradually accelerates, smoothly passing through the

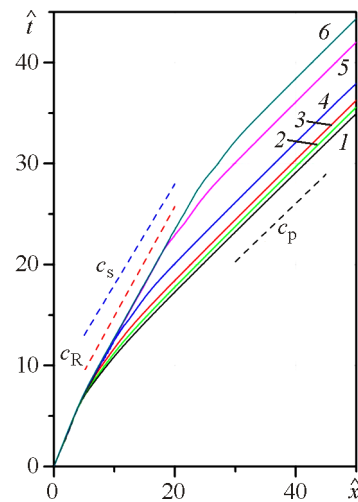


Fig. 3. Hodographs of the differential motion start at different strength parameters of the fault $S = 0.5$ (1), 0.6 (2), 0.7 (3), 0.8 (4), 0.85 (5), and 0.9 (6). The dashed lines show the hodograph slopes for the longitudinal, shear and Rayleigh waves (color online).

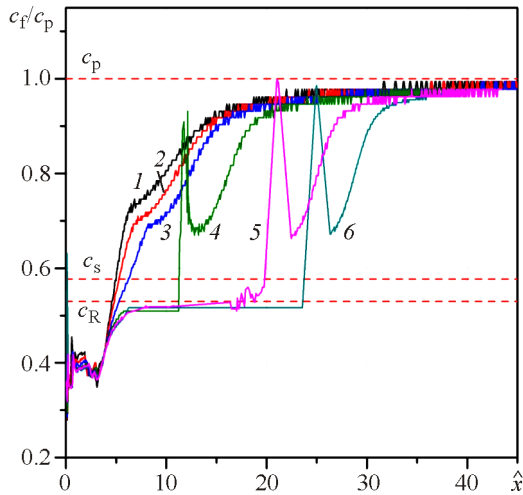


Fig. 4. Variation of the rupture start velocity with distance at different strength parameter of the fault $S=0.5$ (1), 0.6 (2), 0.7 (3), 0.8 (4), 0.85 (5), and 0.9 (6) (color online).

velocity range $C_R < C_f < C_s$, previously considered “forbidden”, and approaches the longitudinal wave velocity C_p . Moreover, the compression wave velocity is achieved in a very short time. At $S \geq 0.8$ (curves 4–6 in Fig. 4), the transition from the sub-Rayleigh to supershear regime is accompanied by a sharp jump in the rupture velocity, which is caused by the nucleation of a “daughter” crack [17, 18].

5.2. Heterogeneous Slip Surface

The next series of calculations were made to simulate the sliding process along a heterogeneous contact. The heterogeneity was formed of zones with

different types of frictional properties in accordance with (2): with weakening (FW, $S=0.6$) and with constant shear resistance equal to the background stress $\tau = \tau_0$ (FS). The slip surface was modeled by alternating velocity-weakening zones of length L_{asp} and stable zones of length Δx . The heterogeneous surface begins at the coordinate $\hat{x} = 10$. The size of FW zones was constant and was set to $\hat{L}_{asp} = 7$. The parameter $\delta = \Delta x / L_{asp}$ was taken as a dimensionless characteristic of the heterogeneous slip surface, which characterizes the ratio of FW to FS zones: the higher the parameter δ , the lower the fraction of weakening zones (asperities).

The differential motion of the fault sides in the FS zone starts at the longitudinal wave velocity. Since friction is always fully mobilized in these zones at $\tau \geq \tau_0$, no additional frictional resistance arises in these zones during sliding acceleration initiated by the dynamic action. Consequently, a weak longitudinal wave propagating along the fault with the strength insufficient to move the locked FW zone causes sliding in FS zones. When analyzing hodographs (Fig. 5), one should keep in mind the completely different response of FW and FS zones of the fault to the rupture propagation.

Rupture propagation in the FS zone is not accompanied by the release of elastic energy stored in the block, and, therefore, the seismic wave associated with the rupture gradually attenuates. If such a rupture meets another FW zone with a higher frictional strength, the rupture can be arrested. This is the only mechanism of rupture arrest within the used model. At small S , the tensile strength is low, and the influ-

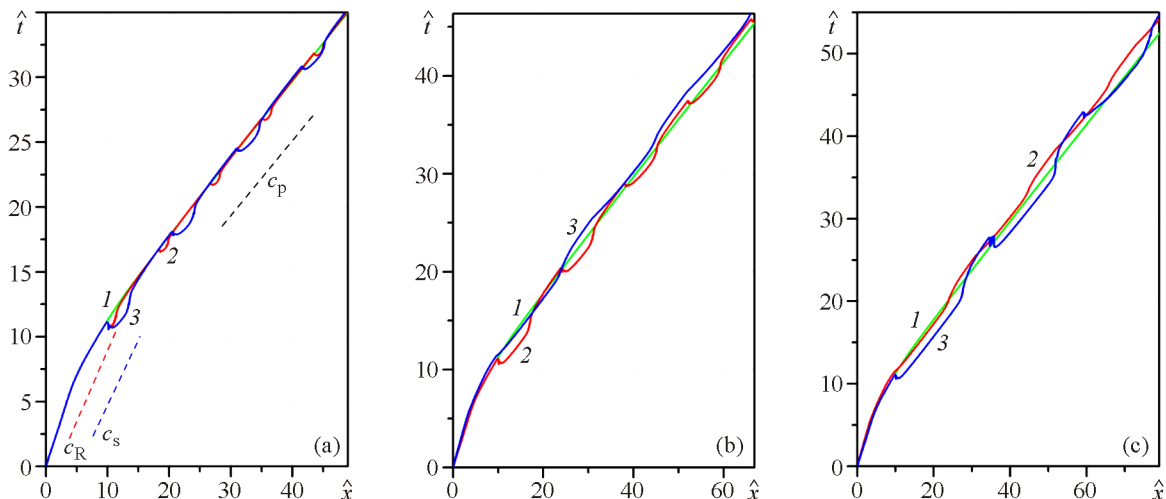


Fig. 5. Hodographs of the differential motion start: a— $\delta=0$ (1), 0.2 (2), and 0.5 (3); b— $\delta=0$ (1), 1 (2), and 2 (3); c— $\delta=0$ (1), 2 (2), and 2.5 (3) (color online).

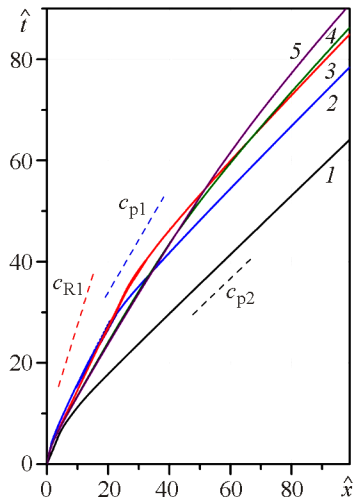


Fig. 6. Hodographs of the differential motion start. $\hat{H} = 0$ (1), 0.3 (2), 0.75 (3), 1.5 (4), and 2.3 (5) (color online).

ence of heterogeneity in the considered range of parameters is weak. As S increases, this influence grows rapidly. Thus, in the case $S=0.8$, the rupture is arrested already at $\delta=2.5$ [18].

5.3. Interface with the Weakening Zone

Another series of calculations was aimed at simulating a rupture along the contact surface with the fracture zone. Unlike the previous calculations with velocity-weakening zones, this model assumes a spontaneous initiation of a rupture, which propagates at a constant prescribed rupture velocity $V_r = V_{\text{init}}$.

In this case, use was made of the simplest fault model, which presents a homogeneous zone of weakened rock of thickness H_j , with the slip plane in its center. The host rock parameters were the density $\rho_0 = 2.992 \times 10^3 \text{ kg/m}^3$, Poisson's ratio $\nu = 0.25$, and longitudinal wave velocity $C_{p2} = 6 \text{ km/s}$. The rock parameters in the weakening zone were $\rho_0 = 2.5 \text{ g/cm}^3$, $\nu = 0.25$, $C_{p1} = 3.35 \text{ km/s}$, and $C_{s1} = 2.5 \text{ km/s}$. The parameter $S = 0.6$. The size of the weakening zone varies in the range $\hat{H} = 0.3\text{--}2.3$.

In the presented series of calculations, the rupture velocity ultimately reaches the longitudinal wave velocity in the block C_{p2} . Moreover, the larger the weakening zone H_j , the farther this occurs from the point of initiation of the rupture. At $\hat{H} > \sim 1.2$, the rupture quickly passes first to the supershear regime in the near-fault zone of weakened rock, and then gradually accelerates to the longitudinal wave velocity in the host block. Due to this, in the initial sec-

tion (sections up to $\hat{x} \sim 50$ in Fig. 6), the rupture can propagate faster along the fault with a wider weakening zone than along the fault with a smaller weakening zone (Fig. 6).

6. CONCLUSIONS

The numerical experiments confirmed the existence of two different mechanisms that control the transition to the supershear regime, in which the rupture velocity exceeds the velocity of the generated seismic shear waves. In most cases, the transition to a supershear rupture occurs due to the rapid but smooth acceleration of the main adhesion zone. The simulation results on this process were discussed. In some cases, the transition occurs due to the temporary formation of a secondary adhesion zone in front of the main crack, which quickly coalesces with the primary adhesion zone. Calculations of this scenario were presented in [18].

The parameter S , which can be called a measure of the fault strength, allows a numerical characterization of the stress state of the contact [17].

In the calculations, the main attention was paid to rupture scenarios at the parameter S in the range $0.4 < S < 0.8$, which corresponds to the so-called “weak” faults. The results demonstrated that, at such values of the fault strength measure S , the rupture velocity continuously increased from the sub-Rayleigh to shear wave velocity and quickly exceeded it without any jump: the fault smoothly passed to the supershear regime.

For relatively “weak” faults, the transition to the supershear regime occurs soon after its initiation. However, for “strong” faults with the parameter S in the range $0.9 \leq S \leq \sim 1.77$, the transition to the supershear regime takes rather more time: first, a daughter crack is initiated, the velocity of which exceeds the range of the Rayleigh wave velocity to the shear wave velocity, and the mother crack continues to propagate at a velocity below the Rayleigh one and only then coalesces with the daughter crack [18].

The calculations demonstrated that the parameter $S \approx 1.8$ was maximum possible for the implementation of a supershear sliding regime along the fault. Above this value, the rupture scenario is typical of the usual sub-Rayleigh regime, and the normal velocity component of the medium displacement prevails [18].

It is very important that the results of such simulation for nonstationary spontaneous ruptures are in no conflict [17] with the classical theoretical solutions

for singular stationary cracks [1, etc.], which stated the presence of a “forbidden” region of rupture velocities. It is obvious that the velocity region $[C_R, C_s]$ is very unstable for nonstationary ruptures: it is very quickly exceeded by the tendency to the compression wave velocity C_p . Ultimately, the only possible rupture velocity is either the compression wave velocity for relatively weak faults or the Rayleigh wave velocity for relatively strong faults.

Like any simulation, the above calculation problem was solved based on a number of assumptions. The use of two-dimensional calculation, linear law of sliding weakening, and plane model of the fault zone significantly simplified the rupture process. However, the analysis of even such idealized model scenarios of sliding along a fault reveals key details of the origin and development of large earthquakes and thus significantly improves the understanding of special features of propagation of dynamic ruptures and emission of seismic waves.

FUNDING

The research was financially supported by Russian Science Foundation (project No. 22-27-00565).

CONFLICT OF INTEREST

The authors of this work declare that they have no conflicts of interest.

REFERENCES

1. Kostrov, B.V. and Das, S., *Principles of Earthquake Source Mechanics*, Cambridge: Cambridge University Press, 1988.
2. Chouneta, A., Valléa, M., Causseb, M., and Courboullex, F., Global Catalog of Earthquake Rupture Velocities Shows Anticorrelation between Stress Drop and Rupture Velocity, *Tectonophysics*, 2018, vol. 733, no. 9, pp. 148–158. <https://doi.org/10.1016/j.tecto.2017.11.005>
3. Bhat, H.S., Dmowska, R., King, G.C., Klinger, Y., and Rice, J.R., Off-Fault Damage Patterns due to Supershear Ruptures with Application to the 2001 Mw 8.1 Kokoxili (Kunlun) Tibet Earthquake, *J. Geophys. Res. B*, 2007, vol. 112, p. B06301. <https://doi.org/10.1029/2006JB004425>
4. Liu, Y. and Lapusta, N., Transition of Mode II Cracks from Sub-Rayleigh to Intersonic Speeds in the Presence of Favorable Heterogeneity, *J. Mech. Phys. Solids*, 2008, vol. 56(1), pp. 25–50.
5. Andrews, D.J., Ground Motion Hazard from Supershear Rupture, *Tectonophysics*, 2010, vol. 493(3-4), pp. 216–221. <https://doi.org/10.1016/j.tecto.2010.02.003>
6. Bizzarri, A. and Das, S., Mechanics of 3-D Shear Cracks between Rayleigh and Shear Wave Rupture Speeds, *Earth Planet. Sci. Lett.*, 2012, vol. 357–358, pp. 397–404. <https://doi.org/10.1016/j.epsl.2012.09.053>
7. Wang, D.D., Mori, J., and Koketsu, K., Fast Rupture Propagation for Large Strike-Slip Earthquakes, *Earth Planet. Sci. Lett.*, 2016, vol. 440, pp. 115–126.
8. Zeng, J., Jiale Ji, Shuyu Chen, and Fucheng Tian, Sub-Rayleigh to Supershear Transition of Dynamic Mode-II Cracks, *Int. J. Eng. Sci.*, 2023, vol. 188, p. 103862. <https://doi.org/10.1016/j.ijengsci.2023.103862>
9. Das, S., Supershear Earthquake Ruptures—Theory, Methods, Laboratory Experiments and Fault Superhighways: An Update, in *Perspectives on European Earthquake Engineering and Seismology*, Ansal, A., Ed., Springer 2015, pp. 1–20. https://doi.org/10.1007/978-3-319-16964-4_1
10. Causse, M. and Song, S.G., Are Stress Drop and Rupture Velocity of Earthquakes Independent? Insight from Observed Ground Motion Variability, *Geophys. Res. Lett.*, 2015, vol. 42(18), pp. 7383–7389. <https://doi.org/10.1002/2015gl064793>
11. Ellsworth, W.L., Celebi, M., Evans, J.R., Jensen, E.G., Kayen, R., Metz, M.C., Nyman, D.J., Roddick, J.W., Spudich, P., and Stephens, C.D., Near-Field Ground Motion of the 2002 Denali Fault, Alaska, Earthquake Recorded at Pump Station 10, *Earthq. Spectra*, 2004, vol. 20, pp. 597–615. <https://doi.org/10.1193/1.1778172>
12. Lyu, M., Chen, K., Changhu Xue, Nan Zang, Wei Zhang, and Guoguang Wei, Overall Subshear but Locally Supershear Rupture of the 2021 Mw 7.4 Maduo Earthquake from High-Rate GNSS Waveforms and Three-Dimensional InSAR Deformation, *Tectonophysics*, 2022, vol. 839, p. 229542. <https://doi.org/10.1016/j.tecto.2022.229542>
13. Li, Q., Wan, Y., Li, C., Tang, H., Tan, K., and Wang, D., Source Process Featuring Asymmetric Rupture Velocities of the 2021, *Seismol. Res. Lett.*, 2022, vol. 93(3), pp. 1429–1439. <https://doi.org/10.1785/0220210300>
14. Abdelmeguid, M., Zhao, C., Yalcinkaya, E., Gazetas, G., Elbanna, A., and Rosakis, A., Revealing the Dynamics of the Feb. 6th 2023 M7.8 Kahramanmaraş/Pazarcik Earthquake: Near-Field Records and Dynamic Rupture Modeling: arXiv:2305.01825 [physics.geo-ph], 2023. <https://doi.org/10.48550/arXiv.2305.01825>
15. Rosakis, A., Abdelmeguid, M., and Elbanna, A., Evidence of Early Supershear Transition in the Feb. 6th 2023 Mw 7.8 Kahramanmaraş Turkey Earthquake: From Near-Field Records: EarthArXiv Preprints, 2023. <https://doi.org/10.31223/X5W95G>
16. Amlani, F., Bhat, H.S., Simons, W.J.F., Schubnel, A., Vigny, C., Rosakis, A.J., Efendi, J., Elbanna, A., and Abidin, H.Z., Supershear Shock Front Contributions to the Tsunami from the 2018 Mw 7.5 Palu Earthquake,

- Geophys. J. Int.*, 2022, vol. 230, pp. 2089–2097. <https://doi.org/10.1093/gji/ggac162>
17. Liu, C., Bizzarri, A., and Das, S., Progression of Spontaneous In-Plane Shear Faults from Sub-Rayleigh to Compressional Wave Rupture Speeds, *J. Geophys. Res. Solid Earth.*, 2014, vol. 119, pp. 8331–8345. <https://doi.org/10.1002/2014JB011187>
 18. Budkov, A.M., Kishkina, S.B., and Kocharyan, G.G., Modeling Supershear Rupture Propagation on a Fault with a Heterogeneous Surface, *Izv. Phys. Sol. Earth*, 2022, vol. 58, no. 4, pp. 562–575.
 19. Bhat, H.S., *Supershear Earthquakes. Theory. Experiments. Observations*, 2020. <https://harshasbhat.github.io/files/Bhat2021a.pdf>
 20. Bao, H., Xu, L., Meng, L., Ampuero, J.P., Gao, L., and Zhang, H., Global Frequency of Oceanic and Continental Supershear Earthquakes, 31 October 2022, *Nature Geosci.* <https://doi.org/10.1038/s41561-022-01055-5>
 21. *Earthquake and Disaster Risk: Decade Retrospective of the Wenchuan Earthquake*, Li, Y.-G., Ed., 2019. <https://doi.org/10.1007/978-981-13-8015-0>
 22. Zhan, Z., Shearer, P.M., and Kanamori, H., Supershear Rupture in the 24 May 2013 Mw 6.7 Okhotsk Deep Earthquake: Additional Evidence from Regional Seismic Stations, *Geophys. Res. Lett.*, 2015, vol. 42, pp. 7941–7948. <https://doi.org/10.1002/2015GL065446>
 23. Yue, H., Lay, T., Freymueller, J.T., Ding, K., Rivera, L., Ruppert, N.A., and Koper, K.D., Supershear Rupture of the 5 January 2013 Craig, Alaska (Mw 7.5) Earthquake, *J. Geophys. Res. Solid Earth.*, 2013, vol. 118, pp. 5903–5919. <https://doi.org/10.1002/2013JB010594>
 24. Bao, H., Ampuero, J.P., Meng, L., Fielding, E., Liang, C., Milliner, C., Feng, T., and Huang, H., Early and Persistent Supershear Rupture of the 2018 Magnitude 7.5 Palu Earthquake, *Nature Geosci.*, 2019, vol. 12. <https://doi.org/10.1038/s41561-018-0297-z>
 25. Okuwaki, R., Yagi, Y., Taymaz, T., and Hicks, S., *Multi-Scale Rupture Growth with Alternating Directions in a Complex Fault Network during the 2023 South-Eastern Türkiye and Syria Earthquake Doublet: Preprint*, 2023. <https://doi.org/10.31223/X5RD4W>
 26. Erdik, M., Tümsa, M.B.D., Pınar, A., Altunel, E., and Zülfikar, A.C., *A Preliminary Report on the February 6, 2023 Earthquakes in Türkiye: Preprint*, 2023. <https://doi.org/10.32858/temblor.297>
 27. Kocharyan, G.G. and Kishkina, S.B., The Physical Mesomechanics of the Earthquake Source, *Phys. Mesomech.*, 2021, vol. 24, no. 4, pp. 343–356. <https://doi.org/10.1134/S1029959921040019>
 28. Das, S. and Kostrov, B.V., Breaking a Single Asperity: Rupture Process and Seismic Radiation, *J. Geophys. Res.*, 1983, vol. 88, pp. 4277–4288.
 29. Rautian, T.G., Determination and Interpretation of Parameters of Earthquake Subfoci, in *Questions of Engineering Seismology*, vol. 29, *Seismic Hazard Studies*, Moscow: Nauka, 1988, pp. 21–29.
 30. Shebalin, N.V., *Strong Earthquakes: Selected Works*, Moscow: Publ. House of the Academy of Mining Sciences, 1997.
 31. Kocharyan, G.G., *Geomechanics of Faults*, Moscow: GEOS, 2016.
 32. Batukhtin, I.V., Budkov, A.M., and Kocharyan, G.G., Features of Initiation and Arrest of a Rupture on Faults with a Heterogeneous Surface, in *Proc. of the V International Conference on Trigger Effects in Geosystems*, 2019, pp. 137–149.
 33. Andrews, D.J., Rupture Velocity for Plane Strain Shear Cracks, *J. Geophys. Res.*, 1976, vol. 81, no. 32, pp. 5679–5687.
 34. Budkov, A.M. and Kocharyan, G.G., Numerical Modeling of Supershear Rupture Propagation on Faults with Homogeneous and Heterogeneous Surfaces, *Dynam. Prots. Geosf.*, 2021, no. 13, pp. 10–19.
 35. Arkhipov, V.N., Borisov, V.A., and Budkov, A.M., *Mechanical Action of a Nuclear Explosion*, Moscow: Fizmatlit, 2003.

Publisher’s Note. Pleiades Publishing remains neutral with regard to jurisdictional claims in published maps and institutional affiliations.